DOI: 10.13009/EUCASS2023-804

On the capillary rise of cryogenic liquids in microgravity: numerical analysis and experiments

D. Fiorini[1,2†], *M. A. Mendez*[1], *D.Seveno*[2] *and A. Gosset*[3]
[1]*von Karman Institute for fluid dynamics, Waterloosesteenweg 72, Sint-Genesius-Rode, Belgium*
[2]*KU Leuven, Dept. of Materials Engineering, Leuven 3001, Belgium*
[3]*Universidade da Coruña, Campus de Esteiro s/n, 15403 - Ferrol, Spain*
[†] domenico.fiorini@vki.ac.be

Abstract

Capillary forces govern the spreading of liquids on solid walls. These forces play a crucial role in microgravity conditions, impacting liquid transport, liquid location in tanks, and the design of fuel systems for space missions. While Computational Fluid Dynamics (CFD) can provide valuable insights on the fluid behaviour, challenges persist in anticipating the gas-liquid interface dynamics in microgravity, especially for low viscosity and volatile cryogenic fluids such as space propellants. In this study, the accuracy of two-phase Volume Of Fluid (VoF) simulations is assessed against a new experimental data-set for a test case involving liquid interface reorientation and capillary rise in a U-shaped divergent tube. The simulations are also compared with an analytical model for the interface motion. The results show that the model and the CFD predict the same macroscopic fluid behaviour. Moreover, the available experimental data allow identifying and tuning the most relevant parameters of the CFD model for a capillary-inertia dominated flow.

1. Introduction

Engineering the wetting behaviour of a liquid in the absence of gravitational forces presents significant challenges [25, 26, 32]. The knowledge of the location of the free liquid/gas interface's in these conditions [27, 39] and the understanding of the wall-to-fluid heat transfer dynamics [29, 36] are fundamental for the design and optimization of cryogenic upper stage tanks and capillary-based propellant management devices (PMDs) [15, 22].

Currently, computational fluid dynamics (CFD) is the primary tool for evaluating PMD performance and predicting the sloshing dynamics in partially filled tanks. One of the simplest approaches to model the gas-liquid interface relies on interface capturing methods, which are formulated for eulerian meshes, and use an advection equation that governs the evolution of an interface function. One of the most popular technique within this framework is the Volume of Fluid (VoF) method, which locates the interface through an indicator function known as the liquid volume Fraction (α). In the algebraic version of VoF solvers, there is no geometrical reconstruction of the interface, and this is why the latter is prone to numerical diffusion. In that sense, VoF methods are often referred to as "diffuse-interface methods". For the computation of the surface tension term, the Continuum-Surface-Force (CSF) model provides a widely accepted methodology [3, 17] while Flux-Corrected Transport (FCT) schemes are used to address the dynamics of the contact line and regulate the interface thickness. In this framework, the accurate computation of the interface curvature plays a key role in the accuracy of the predictions [7].

Despite the conceptual simplicity of diffuse-interface methods, several works [6, 14, 16] have shown that the mixing region of finite thickness at the interface may generate non-physical artefacts, such as parasitic currents, which lead to incorrect predictions of instability growth rates in viscous interfacial flows. Another challenge in VoF simulations of capillary-dominated phenomena is the high sensitivity to mesh resolution. For example, Afkhami et al. [1] show that increased resolutions lead to divergence of the shear stress at the contact line between the free surface and the solid. This is due to the difficulties of discretized techniques to handle the well-known 'non-slip paradox' [20] that must reconcile the no-slip boundary condition at the wall with the relative motion between the contact line and the wall. This numerical issue can be mitigated by replacing the conventional no-slip boundary condition with a partial slip condition allowing a tangential velocity near the contact line, parametrized by the so-called "slip length". However, this adds one more numerical parameter in the computations, whose value cannot always be related to a fully physical scale.

DOI: 10.13009/EUCASS2023-804

Because of “free” parameters such as the slip length or the level of interface compression, numerical tools for simulating wetting phenomena are usually calibrated against prototype case studies. One such case is the capillary rise of liquid in small vertical capillary tubes. It constitutes an ideal test case because it is geometrically simple and because the macroscopic motion of the interface can be described by well-established ordinary differential equation (ODE) models [37]. Building upon this, several authors have investigated experimentally the capillary rise of perfectly wetting liquids in cylindrical tubes subjected to step reductions in gravity within drop-tower setups [11, 33]. However, these experimental works do not provide quantitative information on the interface shape and dynamics. This prevents a detailed validation of CFD simulations.

On the numerical side, Gründing et al. [14] conducted a detailed study of the capillary rise, performing a code-to-code comparison that included an algebraic Volume of Fluid method, among others. For all methods, the authors analyzed the effects of mesh resolution and partial slip boundary conditions, considering various levels of ’numerical slip’ and ’real slip’. By ’numerical slip’, one refers to the practice of setting the non-slip condition on a mesh which has no centroids at the exact wall location, thus tolerating that no cells experiences an exact non-slip. Conversely, in the case of ’real-slip’, the slip condition is imposed in a strict sense. The authors conclude that the ‘numerical slip’ fails to yield mesh-converging results, in contrast to the ‘real-slip’ condition. However, the latter theoretically requires slip lengths of the order of the nano-scale, which would demand prohibitively fine meshes.

In this study, we present a new capillary rise test case designed to produce a capillary-dominated flow only in microgravity conditions. This test case is a variant of the capillary tube, in which the tube is U-shaped to avoid the penetration of liquid at the entrance like in classical capillary rise configurations, and whose radius increases linearly along the axis to accelerate the flow. The test case was investigated during the 78th ESA parabolic flight campaign and characterized using a combination of high-speed quantitative visualization and image velocimetry [9]. The campaign collected detailed data on the gas-liquid interface reorientation and capillary rise. We replicate the experiments with the VoF solver from the OpenFOAM finite volume libraries. Our investigation explores the relationship between mesh resolution and interface compression while incorporating slip-length models to compensate for viscous stress’s divergence and mitigate mesh sensitivity. The relatively long experiment duration and the varying external acceleration provide a unique test case to calibrate the relevant numerical parameters for capillary-dominated simulation.

2. Test case description and model

2.1 Test case

Figure 1a shows on the left a 3D model of the Divergent U-Tube (DUT) configuration considered in this work. On the right, Figure 1b shows the installation of the DUT quartz tube on a robust aluminium structure. The structure consists of two plates joined by four cylindrical beams via M8 screws. A resin is poured into two pockets of the structure to clamp the tube. The system is designed to allow optical access while having sufficient rigidity to avoid vibration, which could result in the cracking of the quartz.

The tube is symmetric with respect to the x-axis and is described using an equivalent cylindrical coordinate system as illustrated by Figure 2. Both the internal and external radius of the tube increase linearly with respect to the curvilinear axis of the tube, identified with ζ, except for the curved part where $|\zeta| < D_u/2$ with $D_u = 40$ mm being the distance between the tube vertical axis. The two sides of the tube are connected with a flexible junction. This prevents leakages and creates a closed environment in which saturated conditions are reached before the experiments begin. The tube is partially filled with a test liquid and in normal gravity conditions a gas-liquid interface is visible on each side of the tube at the same height z.

The DUT configuration holds several advantages both on the experimental and numerical side. The liquid reservoir used in classic capillary rise experiments is replaced by the larger side of the DUT. This minimizes the impact of liquid sloshing occurring during the parabolic flight and the capillary forces on both sides affect the motion of the liquid. The lack of a tube entrance reduces viscous losses due to sudden tube constriction, minimizing the effect of viscous forces on the interface motion and reducing the duration of the viscous-dominated phase of the capillary rise as identified by Stange et al. [33]. On the numerical side, the self contained aspect of the experiments allows imposing boundary conditions unambiguously and the substitution of the tube entrance with a tube bend allows to decrease the uncertainties linked to the identification of the extra viscous losses.

The experiment recordings start with the announcement of the plane being at 40 degrees inclination. Shortly after the announcement, the gravity levels drop from approximately $1.8g$ to approximately $0g$, and the two liquid interfaces begin moving along the axis of the tube due to the unbalanced capillary action of the interfaces. The motion of each interface is recorded with a high-speed camera (model JAY SP-12000-CXP4), acquiring grey-scale images at 300 fps. The active region of the camera sensors is restricted to the central region of size $4096 \times n_{px}$ pixels where the lateral size n_{px} is optimized according to the tube geometry to achieve the highest possible acquisition frequency.

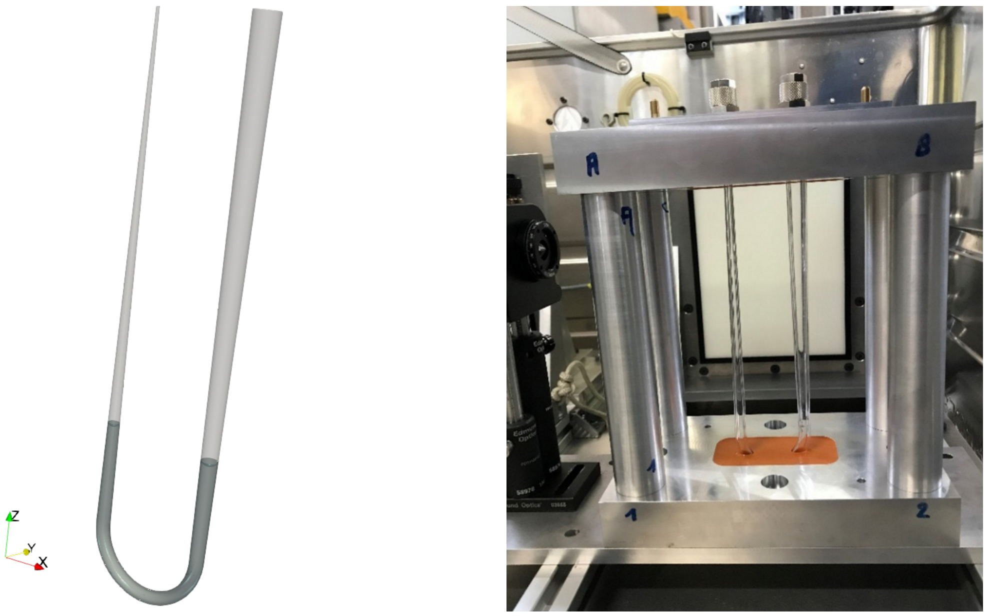

(a) CFD model.

(b) Experimental set-up.

Figure 1: The Figure on the left shows on the left the numerical model of the DUT and on the right the experimental configuration. The latter is enclosed on a rigid structure to avoid resonance vibrations in the quartz.

All cameras mount objectives with 105mm focal lenses and are positioned to capture the full motion of the interface while spanning the largest possible tube length. The meniscus shape is corrected for the optical distortions using the procedure developed by Fiorini et al. [8]. The final pixel size corresponds to $0.013\mu m$.

The test liquid is HFE7200, a perfect wetting liquid used as model fluid for the study of cryogenic propellants. Table 1 reports the fluid properties considered in this work [30]. The reader is referred to [9] for more details on the experimental campaign.

Table 1: Fluid physical properties.

density (ρ)	**dynamic viscosity** (μ)	**surface tension** (σ)
1423.00 kg/m^3	0.64 mPa $\cdot$ s	13.62 mN/m

2.2 1D Integral Model of the Liquid Column

We describe the motion of the liquid's center of mass in the DUT with a 1D integral model balancing the acceleration of the center of mass with friction, gravity and the interface capillary pressure drop. We derive the model assuming a gentle curvature of the tube and a cylindrical coordinate system (ζ, η) with ζ aligned with the tube axis and η aligned along the tube radius as illustrated in Figure 2. We integrate along the liquid domain the contributions of all forces to obtain the following second-order non-linear ODE:

$$\rho V_l \ddot{Y} = -F_g(Y, a(t)) + F_v(\dot{Y}, Y) + F_c(\dot{Y}, Y)\,, \tag{1}$$

where Y, $\dot{Y}$ and $\ddot{Y}$ are respectively the position, the velocity and the acceleration of the liquid column's center of mass along the tube axis $\zeta \in [-L/2, L/2]$. On the right-hand side, F_g denotes the gravitational force acting on the center of mass of the liquid column, F_v denotes the viscous shear that applies to the liquid column, and F_c denotes the net result of the capillary pressure due to the two gas-liquid interfaces on the opposite sides of the liquid column. V_l is the volume of liquid within the tube and $a(t) = [a_x(t), a_y(t), g(t)]$ is the local acceleration of the tube.

We denote with $z_A(Y)$ and $z_B(Y)$ the position of the two interfaces along the curvilinear coordinate ζ, with $z_A(Y)$ corresponding to the smallest side of the tube and $z_B(Y)$ to the largest. The gravity term in (1) results from the contribution of both the height difference $|z_A(Y)| - |z_B(Y)|$ and the local acceleration $a(t)$.

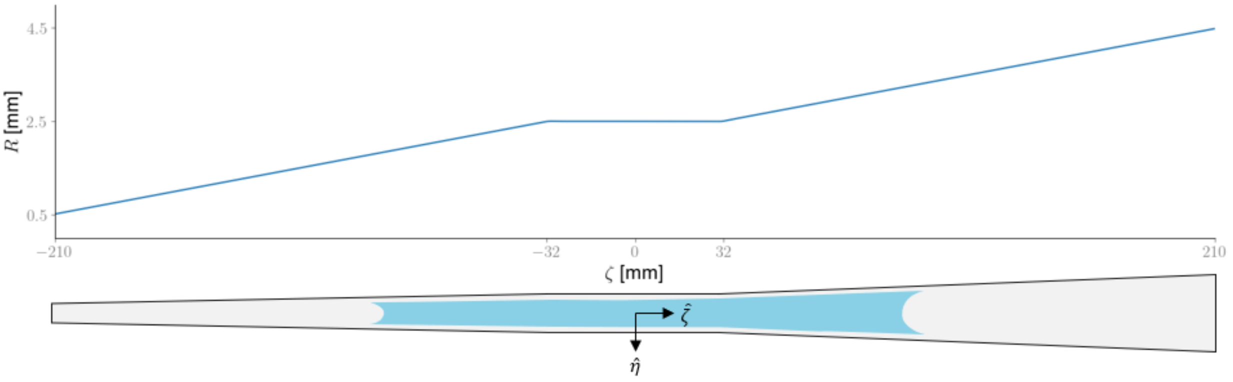

Figure 2: On top, the figure shows the evolution of the internal radius of the tube along with the curvilinear axis ζ. Below, the sketch illustrates the equivalent cylindrical coordinate system for the DUT where gentle curvature of the tube is assumed, i.e. we consider straight streamlines and neglect small variations due the curvature of the tube bend.

The viscous force term in (1) results from the integration of the viscous term in the Navier-Stokes equations, here denoted as τ, both across the liquid column length $z_B(Y) - z_A(Y)$ and the radial direction η:

$$F_v(\dot{Y}, Y) = \int_{z_A(Y)}^{z_B(Y)} \int_0^{R(\zeta)} \tau \, 2\pi\eta \, d\eta \, d\zeta + C_U \,. \tag{2}$$

C_U accounts for the viscous losses in the U-bend. Ghobadi and Muzychka [12] provides an extensive list of empirical correlations for laminar flow in curved ducts. In this work, the value of C_U was calculated from the correction proposed by Itō [21]. Assuming axisymmetric flow, the viscous term τ can be written as

$$\tau = \mu \left[\frac{1}{\eta} \frac{\partial v}{\partial \eta} + \frac{\partial^2 v}{\partial \eta^2} + \frac{\partial^2 v}{\partial \zeta^2} \right] \tag{3}$$

where $v = v(\zeta, \eta, t)$ is the axial velocity of the liquid at the coordinate ζ, η. In normal gravity conditions ($g = 9.8m/s^2$) and for small diameters, classic capillary rise models assume a Poiseuille velocity profile at each axial position of the channel (see for example [40]). Consequently, the velocity profile v can be written as

$$v(\zeta, \eta, t) = 2V(\zeta, t) \left(1 - \frac{\eta^2}{R(\zeta)^2} \right) , \tag{4}$$

where V denotes the mean velocity and $R(\zeta)$ the radius of the channel as a function of the channel axial coordinate.

The capillary term in (1) is modelled as the net sum of the pressure drop at the two interfaces. The latter results from the integration of Laplace equation at each interface, for which we assume spherical cap with constant curvature $2/R_s$ with $R_s(\zeta) \approx R(\zeta)/cos(\theta_D)$. Thus, the capillary pressure term reads:

$$F_c(\dot{Y}, Y) = 2\pi\sigma(R(z_A)cos(\theta_A) - R(z_B)cos(\theta_B)), \tag{5}$$

where θ is the contact angle between the gas-liquid interface and the solid surface of the tube. The contact angle results both from the thermodynamics of the system [13, 31] and the kinematic properties of the contact line (dynamic contact angle, θ_D) [5]. Numerous investigations have characterized the dynamic contact angle in steady viscous dominated configurations [3, 4, 19, 23, 24, 34, 35]. However, the validity of these formulations for inertia dominated test-cases is still under debate [8]. In this work, a preliminary characterization showed that the contact angle varies very little compared to the static value. Consequently, as a first approximation we use a zero contact angle for both interfaces.

We use a fifth-order explicit Runge-Kutta method to solve the integral model (1) using Python's initial value problem solver (scipy.integrate.odeint) starting from the equilibrium position Y_{eq} (obtained by setting $\ddot{Y} = \dot{Y} = 0$ in (1)), due to the balance between gravity and capillary forces, and $\dot{Y} = 0$. We thus compare experiments and CFD in terms of the average height of the liquid column, defined as

$$\bar{h}(t) = -(z_a(Y(t)) - z_a(Y_{eq})) \,. \tag{6}$$

DOI: 10.13009/EUCASS2023-804

3. CFD Methodology

We use the open-source CFD package OpenFOAM to simulate the test case described in this work and reproduce the experimental behavior. The core of the model consists in the VoF solver interFoam modified to read an input file for the accelerations experienced by the DUT for each experimental recording. The solver includes also a user defined dynamic contact angle model. However, in this work the contact angle is kept constant and equal to zero (perfect wetting fluid) to reduce the number of free parameters under investigation.

InterFoam 2112 solves the incompressible, two-phase Navier-Stokes equations, accounting for mass and momentum conservation in each phase. The governing equations are discretized using a finite volume approach. We consider here an unsteady, laminar, isothermal and incompressible two-phase flow. The Volume of Fluid (VoF) method is employed to capture the fluid interface and the interaction between different phases. Following discretization, the local fluid properties are computed as a weighted average of the properties of the liquid and the gas, depending on α, and the volume fraction transport is solved by an advection Equation 7 [18, 38]. Therefore, the cells intersected by the interface are characterized by a value of α between 0 and 1. The surface tension contribution is computed using Continuum-Surface-Force (CSF) model, wherein the surface tension force is regularized by a delta function derived from the volume fraction

$$\frac{\partial \alpha}{\partial t} + \nabla \cdot (\mathbf{U}\alpha) + \nabla \cdot (\mathbf{U_c}\alpha(1-\alpha) = 0\,, \tag{7}$$

with $\mathbf{U} = \mathbf{U_l}\alpha + \mathbf{U_g}(1-\alpha)$ and $\mathbf{U_l}$ being the velocity of the liquid phase and $\mathbf{U_g}$ the velocity of the gas phase. The third term of (7) is an additional artificial compression term which depends on the parameter $\mathbf{U_c}$ defined as:

$$\mathbf{U_c} = C_\alpha |\mathbf{U}| \frac{\nabla\alpha}{|\nabla\alpha|}\,. \tag{8}$$

This term reduces the numerical diffusion of the volume fraction field by introducing an artificial compression in the volume fraction equation and compressing the α profile in the direction normal to the fluid interface. The Interface Compression (IC) coefficient C_α adjusts the compressive effect, with no compression for $C_\alpha = 0$. However, the magnitude of the compression depends also on the mesh resolution. There is no universal strategy to set the value of C_α. Deshpande et al. [6] noted parasitic currents produced by the IC method in surface tension dominated flows. In this work, we observed also that high values of C_α (≈ 1) introduce an additional (small) pressure drop at the interface which in turns alters the dynamics of the flow. Consequently, for the simulations here presented we kept a small value for $C_\alpha = 0.01$.

The essence of the VoF method implemented in the solver interFoam lies in the fact that the interface is not computed explicitly, but is captured based on the volume fraction field. Since the volume fraction values are between 0 and 1, the interface boundary is not located accurately, however, it occupies a thin region in the vicinity of which a sharp interface boundary must exist. The effect of surface tension is modeled with a singular source term in the momentum balance at the interface and is computed based on the continuous surface force model adapted from [2] which reads as:

$$f_\sigma = \sigma\kappa\nabla \cdot \alpha\,, \tag{9}$$

where σ is the liquid-vapor surface tension and κ is the curvature of the interface defined as:

$$\kappa = -\nabla \cdot \left(\frac{\nabla\alpha}{|\nabla\alpha|}\right)\,. \tag{10}$$

Table 2 summarizes the discretization schemes used for this test case. Second-order discretization schemes were used for the spatial terms and a second-order scheme for the time discretization. To ensure a stable solution an adjustable time step was used with a maximum Courant number of 0.5. This gives a typical time step of $\Delta t = 10^{-4}$ s. The pressure-velocity coupling is resolved using a PIMPLE algorithm with three non-orthogonal correctors.

The computations were run in parallel in 64 Intel Xeon Ice Lake 8352Y CPUs at the Centro de Supercomputacion de Galicia (CESGA). The time required for 10 s of real flow computation ranges between 50 and 100 h according to the mesh.

3.1 Test case discretization

The base grid consists in a structured mesh, which is graded towards the pipe walls. We use a standard O-grid configuration transversal to the tube axis to achieve a high degree of mesh orthogonality. In order to capture accurately the interface shape, we use Adaptive Mesh Refinement (AMR) based on the Volume Fraction scalar field. The mesh

DOI: 10.13009/EUCASS2023-804

Table 2: Discretization schemes used.

Term	Discretization scheme
$\partial/\partial t$	Cranck-Nicholson 0.5
$\nabla()$	Gauss linear
$\nabla\cdot(\rho\phi\mathbf{U})^{\dagger}$	Gauss linearUpwind grad(U)
$\nabla\cdot(\phi\alpha)$	Gauss vanLeer
$\nabla\cdot(\alpha(1-\alpha)\phi_r)$	Gauss vanLeer
$\nabla^2()$	Gauss linear corrected
interpolation	linear
normal gradient	corrected

† ϕ surfaceScalarField

Table 3: Solution method for α, pressure and velocity.

Parameter	Solver	Smoother	Tolerance
α	smooth solver	Gauss-Seidel	$1.e-8$
P	GAMG	DIC	$1.e-8$
U	smooth solver	Gauss-Seidel	$1.e-6$

is refined dynamically in the regions with $0.01 < \alpha < 0.99$. The refinement is performed using 3 refinement steps and 2 buffer layers. Based on an initial mesh sensitivity study, Table 4 shows the 3 mesh configurations used for the performed simulations. We characterize each mesh by the resolution (before AMR) in the axial, peripheral and radial direction ζ, β, η. Consequently, we define the respective cell dimensions adjacent to the wall boundary $\delta_\zeta, \delta_\beta, \delta_\eta$ with $\delta_\beta, \delta_\eta$ holding a variable size along the tube axis. To characterize each mesh, we use a normalized notation with $\delta^*_\beta = \delta_\beta/R(\zeta)$ and $\delta^*_\eta = \delta_\eta/R(\zeta)$. The axial resolution in the curved part of the tube is kept at $\delta_{\zeta,bend} = 0.5$ mm for all test cases. A picture of the mesh layout at the gas-liquid interface is shown in Fig. 3 before mesh refinement in Fig. 3a and after mesh refinement in Fig. 3b.

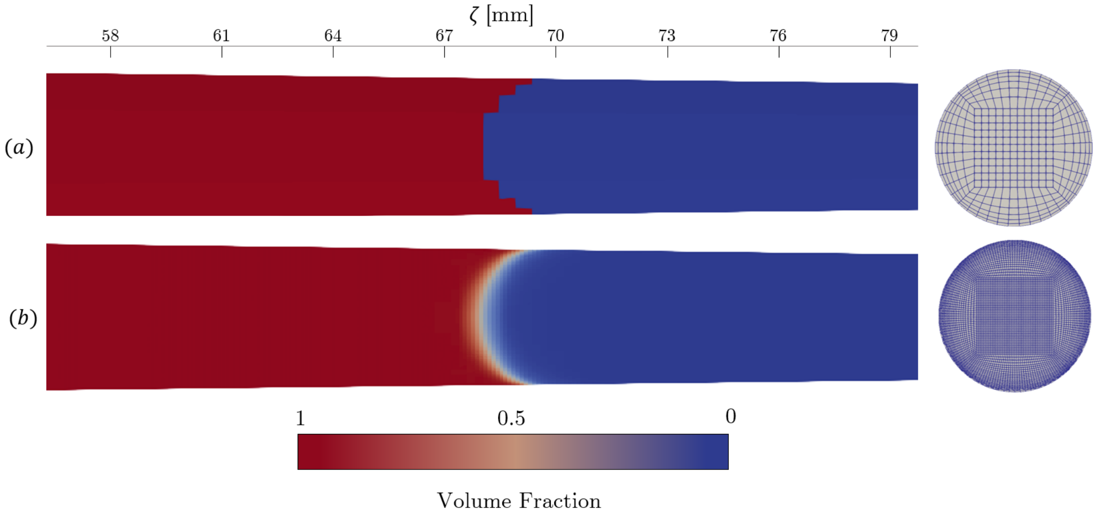

Figure 3: Simulation setup for the simulation for Mesh $n°2$ before AMR (a) and after (b).

3.2 Simulation conditions

Assuming that the solid wall boundary condition applies to each wall of the tube, we use a no-penetration boundary condition and a 0° liquid-solid contact angle for the wall boundaries. We use a partial slip boundary condition at the

DOI: 10.13009/EUCASS2023-804

Table 4: Mesh configurations analized[†].

	$\delta^*_\eta \cdot 100$	$\delta^*_\beta \cdot 100$	δ_ζ [mm]
Mesh $n°1$	4.9	16	0.6
Mesh $n°2$	3.7	14	0.5
Mesh $n°3$	2.4	11	0.4

[†] Before AMR

wall. In the OpenFOAM source code, this is imposed by defining the parameter Value Fraction (VF) as:

$$VF = \frac{\delta_\eta/2}{\delta_\eta/2 + L}, \tag{11}$$

where L is the Navier slip length and $L = 0$ ($VF = 1$) corresponds to the usual no-slip boundary condition. In this work, we characterize each test case by using the dimensionless ratio $L^* = L/R$, which is kept constant for the entire geometry. Recalling the definitions of the previous section, this is calculated as:

$$L^* = \frac{\delta^*_\eta(1 - VF)}{2VF}. \tag{12}$$

At the two tube entrances, a zero gradient boundary condition for the α scalar field and fixed value for the pressure are imposed. For the outflow, a zero-gradient condition is set for the velocity, while for the inflow the velocity is obtained from the patch-face normal component of the internal-cell value (*pressureInletOutletVelocity*). The simulation begins with the liquid phase occupying the bottom part of the tube, and with the gas-liquid interface on each side having an initial position of respectively $z_A = -69.5$ mm and $z_B = 68.7$ mm. The micro gravitational acceleration is oriented vertically and downwards, from the tube entrances towards the bottom part of the bend. The simulation starts when the measured vertical acceleration reaches the value of $a_z = 5.10^{-1}\ g$, with $g = 9.81\ m/s^2$. This allows reducing the computational time since the experimental interface starts oscillating only when $a_z < 10^{-1}\ g$, with the main capillary rise impulse occurring when $a_z < 10^{-3}\ g$.

4. Results

We present the test case and a preliminary analysis of the models in section 4.1. Section 4.2 focuses on the analysis of the sensitivity of the CFD to the mesh and the imposed slip length.

4.1 Test case overview and preliminary analysis

Fig. 4 shows the envelope of the experimental acceleration profiles $a(t) = (a_x(t), a_y(t), a_z(t))$ corresponding to the $\approx$ 40s of recording across the selected parabola. The Figure shows the vertical gravitational acceleration starting at hyper-gravity conditions with $a_z \approx 2g$ at the beginning of the recordings and then dropping to the microgravity level for the majority of the experiment. The experiment terminates when hyper-gravity is reestablished towards the end of the parabola. On the same plot, Fig. 4 shows also the lateral accelerations due to the parabolic flight. The strongest variations occurs in $a_y(t)$ while the $a_x(t)$ appears as a relatively flat profile. With the DUT aligned with the x-axis, the component $a_y(t)$ appears to play a negligible role on the motion of the liquid interface and hence is neglected by the model (1). On the other hand, the component $a_x(t)$ cannot be discarded. In the CFD-VoF simulations the three components of external acceleration are considered. For the following analysis we consider the portion of the experiment highlighted in Fig. 4. This region starts at $a_z = 0.5g$, considered to be the initial instant $t_0 = 0s$, and ends at $t = t_0 + 10s$ where the gas liquid interface leaves the Field of View (FoV) observed by the camera. The chosen t_0 allows capturing the relevant dynamics of the simulation and leaves enough time for the interface shape to adapt to the gravitational field before any motion is triggered.

The comparison between the predictions of the integral model in (1), the CFD and the experimental data is shown in Figure 5 in terms of average column height in (6). Interestingly, model and CFD agree remarkably well but strongly disagree with the experimental results. The departure between numerical predictions and experiments become particularly evident after $t \approx 3$s, once the microgravity is well established. Both models fail to predict the inception of the liquid rise and end up predicting the opposite evolution.

A meticulous sensitivity analysis was conducted on the various terms of (1) to explain the reason for the miss-match. This will be reported in the extended version of this work [10]. Remarkably, this investigation revealed that

DOI: 10.13009/EUCASS2023-804

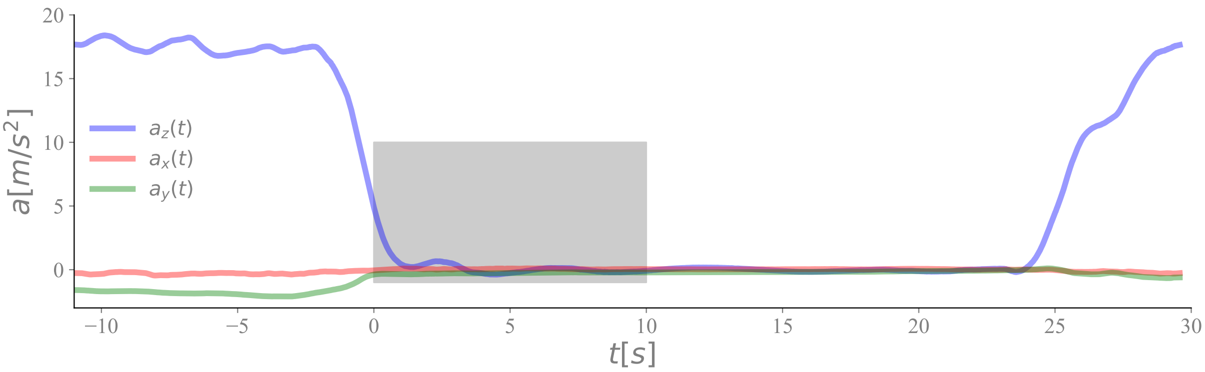

Figure 4: Test-case acceleration as measured during the experimental campaign. The region highlighted shows the simulated time of the experiment.

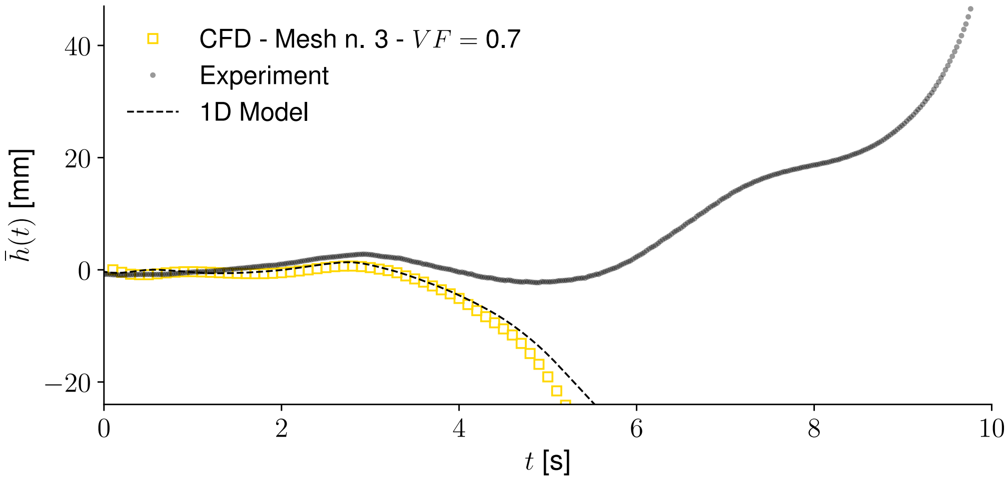

Figure 5: Comparison of the experimental position of the rising gas liquid interface with the CFD and the 1D-ODE model results in absence of corrective term for the capillary effects.

the only solution to restore the agreement was to double the surface tension of the fluid, thus de facto doubling the role of capillary forces. This revealed essential on the initial stages of the flow and particularly in the motion onset; once the motion is established, this artificial correction becomes irrelevant. The fact that both the CFD and the integral model agree with the need for this artificial correction is particularly puzzling and no justification has been currently found. To verify that such correction is indeed artificial, additional measurements of surface tension were performed using 0.1 mm quartz capillary tubes (HR6-128 Hampton Research) and the same HFE7200 sample employed in the experiment. Comparing the steady height of the liquid with the established Jurin's law [28] demonstrated that the surface tension of HFE7200 is the one provided in Table 1. Furthermore, extensive testing of the models' sensitivity confirmed that variations of liquid properties within the range of ±10% from those listed in Table 1 cannot explain the behavior observed in the experiment. Finally, pressure measurements acquired during the experiment using AMS 5812-0015-D pressure transducers were sufficient to discard the presence of any additional pressure gradient in the gas phase.

While a more detailed focus on the origin of this discrepancy is left to future works, we here focus on the impact of numerical parameters such as slip length and mesh resolution on the dynamics of the liquid column. To maintain a comparison with the experimental data the surface tension is doubled in all computations.

Fig. 6 shows an overview of the CFD simulation through snapshots of the region of the tube occupied by the fluid at selected time steps. The boundary of the interface is identified with the isosurfaces $\alpha = 0.5$. The Figure shows that even a few seconds after the gravity level dropped below $0.5g$, the hydrostatic pressure gradient still dominates the liquid flow. Later, the capillary pressure gradient appears clearly visible and shows a decreasing pressure moving from

DOI: 10.13009/EUCASS2023-804

the large side of the tube towards the small side. Towards the end of the simulation, the pressure gradient in the liquid partially reduces; this is probably linked to the progressive flattening of the interface due to the acquired inertia as the liquid accelerates in the small side of the tube, while the interface on the largest side moves slower and keeps a more concave shape yielding a higher pressure drop.

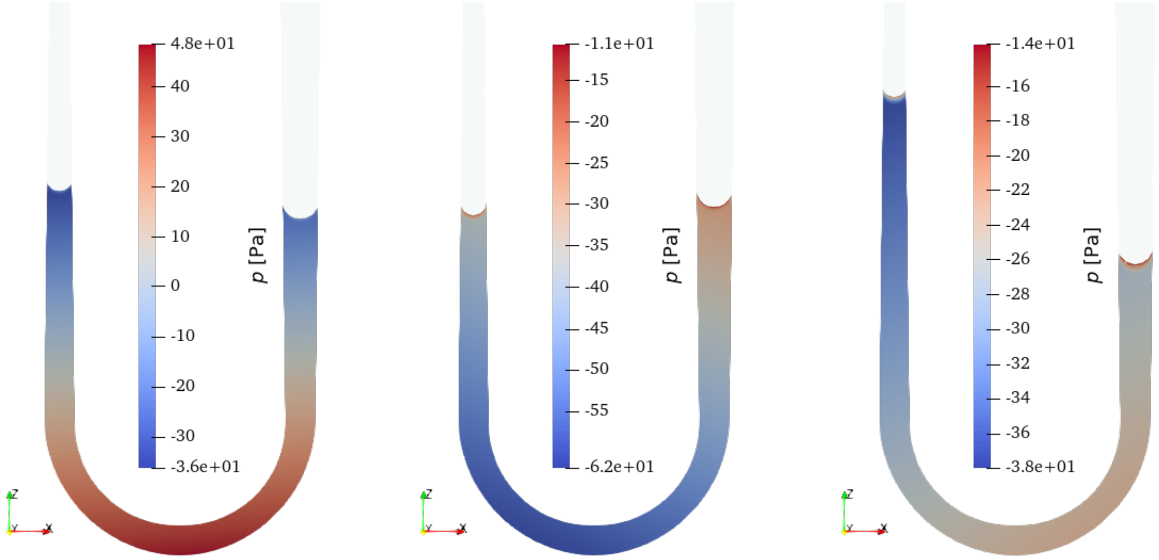

t=2s. t=5s. t=8s.

Figure 6: Snapshots of the simulation and pressure field where $\alpha > 0.5$.

4.2 Calibration of the simulation

A mesh dependence study was conducted for the three meshes summarized in Table 4. Figure 7 shows a comparison between the rise of the experimental interface in the small tube side against the rise predicted by the model (1) and the VoF simulations with no-slip boundary condition, i.e. the effective slip length is proportional to the mesh size [14]. Fig. 7 shows the rising height based on the $\alpha = 0.5$ iso-surface, while the uncertainty on the interface position is shown with the corresponding upper and lower limits obtained for $\alpha = 0.05$ and $\alpha = 0.95$.

The comparison shows a substantial dependency of the CFD simulations on the mesh resolution. The finest mesh $n°3$ clearly introduces an additional source of viscous dissipation at the contact line and hence a higher resistance to the capillary motion. The meshes $n°1$ and $n°2$ yield similar results. The mesh $n°1$ displays a much larger numerical diffusion which appears in the larger range of uncertainty on the interface location. However, all computations appear to follow closely the capillary rise profile predicted by means of the 1D model (1) during the first 4s of the simulation. After $t = 4$, each simulation develops differently as the balance of the capillary forces with external accelerations becomes dominant.

Following Gründing et al. [14], we now investigate the mesh sensitivity with the Navier slip condition at the solid wall. The results are displayed analogously to Fig. 7 in Fig. 8. As expected, the mesh dependency is reduced when the Navier slip model is employed. Mesh convergence seems to be reached with the finest mesh $n°3$, which shows a much reduced viscous dissipation. The results are also in better agreement with the experimental interface position. Interestingly, the prediction of the ODE model follows closely the results of the CFD simulation.

To quantitatively compare the simulations with the experiment, the error on the unsteady evolution of the interface height in each simulation is computed by defining an error metric as in (13):

$$J = \frac{1}{t(n_t)} \sqrt{\sum_{i=1}^{n_t} \left(\bar{h}_{CFD}(t(i)) - \bar{h}_{EXP}(t(i))\right)^2 + \left(\dot{\bar{h}}_{CFD}(t(i)) - \dot{\bar{h}}_{EXP}(t(i))\right)^2 t(i)^2} \,. \tag{13}$$

Where $\bar{h}_{CFD}$ and $\bar{h}_{EXP}$ are defined according to (6). n_t represents the number of time step compared. In contrast to similar metrics, (13) compares also the slopes of both the experimental and numerical capillary rise profiles, allowing

DOI: 10.13009/EUCASS2023-804

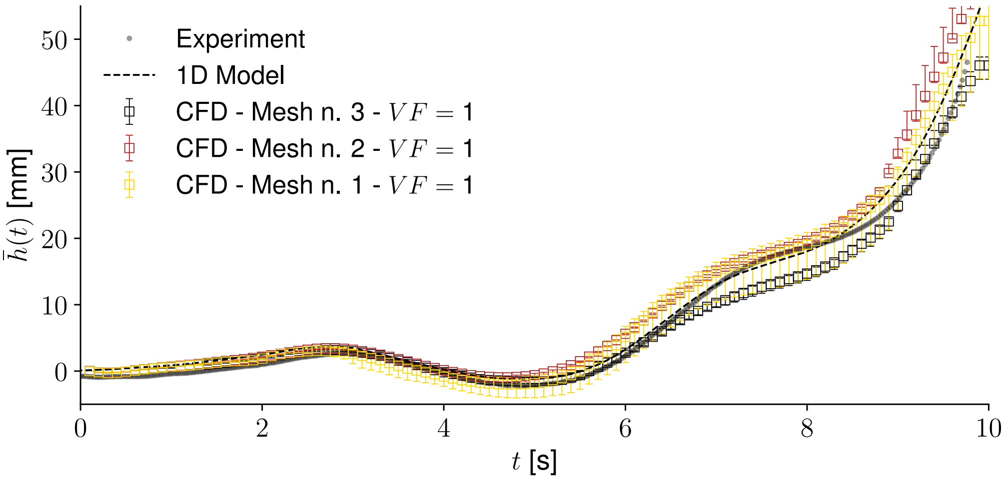

Figure 7: Comparison of capillary rise profile with CFD results obtained with different meshes.

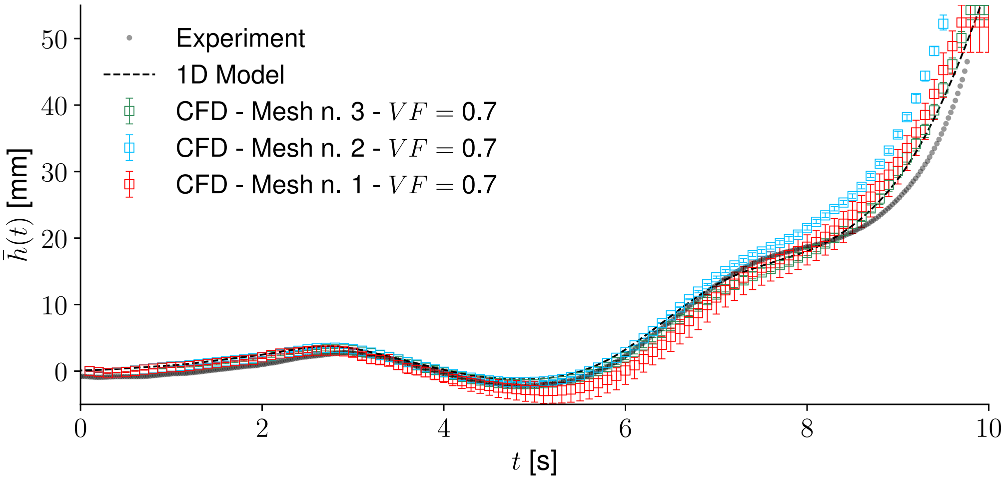

Figure 8: Comparison of capillary rise profile with CFD results obtained with different Value Fraction.

to better visualize ambiguous comparisons. This is the case of Fig. 7 where the comparison of the mesh $n°3$ and $n°2$ yields similar results when assessed only in terms of interface position. Using (13), Fig. 9 shows an overview of the simulations performed for each of the meshes in Table 4 and for different slip lengths L^*. Fig. 9 shows that the agreement of the simulation with the experimental data improves with increasing slip length for all the meshes analyzed.

For the following analysis, we consider the simulation obtained for the mesh $n°3$ with $L^* = 5.10^{-3}$. Fig. 10 compares the experimental and numerical interfaces. On top, the figure shows the experimental interface (after optical correction) observed on the small tube side and on the bottom the numerical result obtained at the corresponding time step. The latter shows also the velocity field in the liquid phase and the velocity vectors computed in a moving reference frame with the velocity of the interface. Both series shows that the interface shape is qualitatively well predicted. Concerning the velocity fields, a parabolic velocity profile is visible a few millimeters below the interface. The distance from the interface where the velocity profile ceases to be parabolic increases as the liquid column accelerates. Near the interface, the computed velocity fields appears often strongly disturbed, which is due to the influence of the interface itself, but also to the numerical dissipation caused by the transition from a relatively coarse mesh in the core of the liquid column towards the refined mesh in the vicinity of the interface.

Finally, Figure 11 compares the numerical interface shape for $\alpha = 0.5$ against the experimental one. Both series are fitted with a spherical cap model with zero contact angle. The different cases show an almost constant shape during most of the simulation, with the exception of the last snapshots. As the interface accelerates, a slight flattening of the

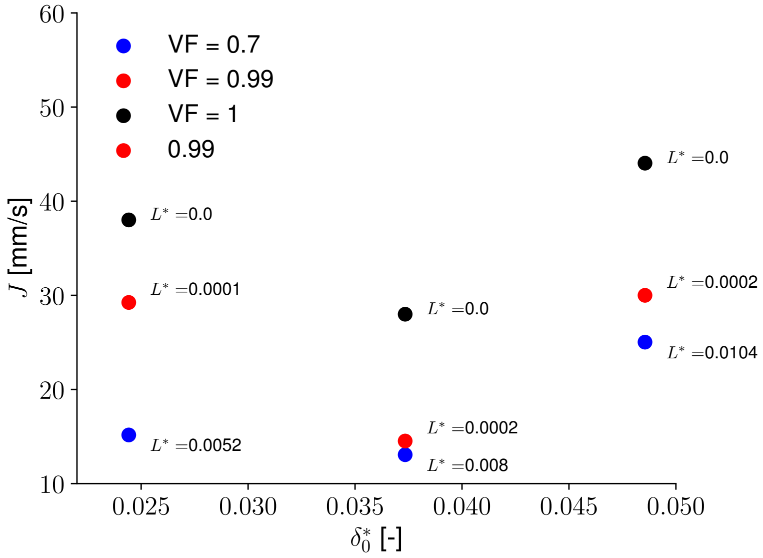

Figure 9: Comparison of capillary rise profile with CFD result.

interface starts occurring at $t = 9.5$ s. This is due to the increased inertia of the flow which dominates the interface behaviour at the later stages of the experiment. Additionally, the numerical interface shows also a slight difference with respect to the experiment due to the different position along the tube predicted by the simulation.

5. Conclusions

In this study, we analyzed the dynamics of a capillary rise in a novel divergent U-tube configuration under microgravity conditions. This test case was designed to produce a capillary driven flow due to the different radii on the two sides of the tube. We assessed the performances of OpenFoam's VoF solver interFoam and a 1D integral model in reproducing the experimental results collected in a dedicated parabolic flight campaign. The objective of this study was to quantify the impact of "free" numerical parameters, such as mesh resolution and the slip length, in the prediction of VoF simulations with no interface reconstruction.

The results showed that the CFD agrees with the integral model but not with the experimental data unless the weight of capillary forces is artificially doubled. A Value Fraction of 0.7 for partial slip was shown to lead to mesh convergent solutions and a good matching with the integral model. Additionally, it was observed that higher Value Fractions (indicative of smaller slip lengths) led to a noticeable reduction in the dynamics of liquid rise, progressively making the CFD solution deviate from the integral model. Future work will investigate the discrepancy with experimental data while also testing the impact of the imposed slip length and dynamic contact angle boundary condition.

6. Acknowledgments

D. Fiorini is supported by Fonds Wetenschappelijk Onderzoek (FWO), Project number 1S96120N. This work was supported by the ESA and BELSPO via the Prodex program and by the ESA-GSTP "Physical and Numerical Modeling of cryogenic sloshing for Space applications" (Contract No. 4000129315/19/NL/MG). We would like to thank also Novaspace for their support and for the fruitful discussions. The authors also wish to thank the CESGA (FinisTerrae III) for the computational resources and the technical support.

References

[1] Shahriar Afkhami, Stephane Zaleski, and Markus Bussmann. A mesh-dependent model for applying dynamic contact angles to vof simulations. *Journal of computational physics*, 228(15):5370–5389, 2009.

[2] CH Bosanquet. Lv. on the flow of liquids into capillary tubes. *The London, Edinburgh, and Dublin Philosophical Magazine and Journal of Science*, 45(267):525–531, 1923.

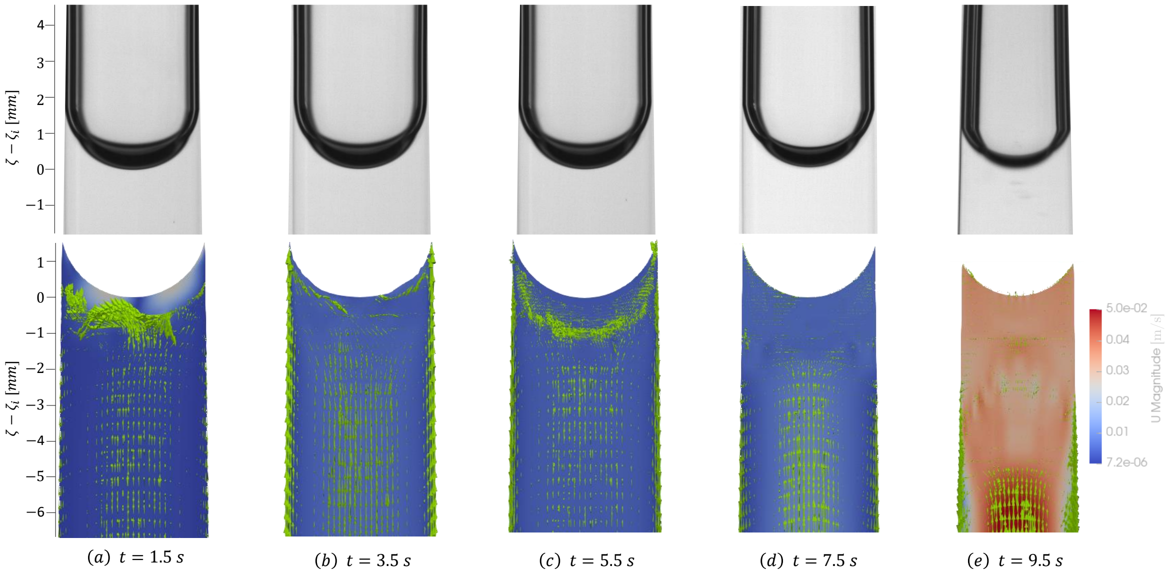

Figure 10: Comparison of 5 snapshots of the gas-liquid interface from the experiments with the numerical prediction obtained for the corresponding time step. The vertical scale of both series is shifted with the central position of the interface ζ_i. The numerical results show also contours of velocity magnitude and 2D vector fields obtained for a moving reference frame with the the meniscus velocity.

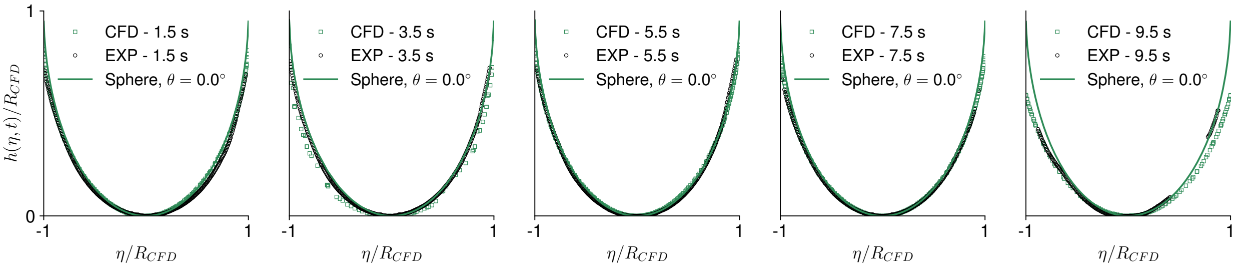

Figure 11: Comparison of the interface shape and the corresponding numerical prediction for 5 time steps. The expected spherical cap is also shown for each plot. Each axis is scaled with the radius of the tube at the contact line of the numerical simulation R_{CFD}.

[3] Jeremiah U Brackbill, Douglas B Kothe, and Charles Zemach. A continuum method for modeling surface tension. *Journal of computational physics*, 100(2):335–354, 1992.

[4] RG Cox. The dynamics of the spreading of liquids on a solid surface. part 1. viscous flow. *Journal of Fluid Mechanics*, 168:169–194, 1986.

[5] PG De Gennes, X Hua, and P Levinson. Dynamics of wetting: local contact angles. *Journal of fluid mechanics*, 212:55–63, 1990.

[6] Suraj S Deshpande, Lakshman Anumolu, and Mario F Trujillo. Evaluating the performance of the two-phase flow solver interfoam. *Computational science & discovery*, 5(1):014016, 2012.

[7] Jean-Baptiste Dupont and Dominique Legendre. Numerical simulation of static and sliding drop with contact angle hysteresis. *Journal of Computational Physics*, 229(7):2453–2478, 2010.

[8] D. Fiorini, M. A. Mendez, A. Simonini, J. Steelant, and D. Seveno. Effect of inertia on the dynamic contact angle in oscillating menisci. *Physics of Fluids*, 34(10):102116, 2022.

DOI: 10.13009/EUCASS2023-804

[9] D. Fiorini, L. Carbonnelle, A. Simonini, J. Steelant, D. Seveno, and M. A. Mendez. Characterization of a capillary driven flow in microgravity by means of optical technique. *Multiphase Science and Technology*, 2023, Under review.

[10] D. Fiorini, A. Simonini, J. Steelant, D. Seveno, and M. A. Mendez. Capillary driven flows in absence of gravity. Under preparation.

[11] Jens Gerstmann and Michael E Dreyer. The dynamic contact angle in the presence of a non-isothermal boundary condition. *Microgravity Science and Technology*, 19:96–99, 2007.

[12] Mehdi Ghobadi and Yuri Stephan Muzychka. A review of heat transfer and pressure drop correlations for laminar flow in curved circular ducts. *Heat Transfer Engineering*, 37(10):815–839, 2016.

[13] J.W. Gibbs. *The Collected Works of J. Willard Gibbs, vol. I, Thermodynamics, pp. 314-331.* Yale Univ. Press, New Haven, 1928.

[14] D Gründing, M Smuda, T Antritter, M Fricke, D Rettenmaier, F Kummer, P Stephan, H Marschall, and D Bothe. A comparative study of transient capillary rise using direct numerical simulations. *Applied Mathematical Modelling*, 86:142–165, 2020.

[15] J. W. Hartwig. Propellant management devices for low-gravity fluid management: past, present, and future applications. *Journal of Spacecraft and Rockets*, 54(4):808–824, 2017.

[16] Dalton JE Harvie, MR Davidson, and Murray Rudman. An analysis of parasitic current generation in volume of fluid simulations. *Applied mathematical modelling*, 30(10):1056–1066, 2006.

[17] Johan A Heyns and Oliver F Oxtoby. Modelling surface tension dominated multiphase flows using the vof approach. In *6th European Conference on Computational Fluid Dynamics*, pages 7082–7090, 2014.

[18] Cyril W Hirt and Billy D Nichols. Volume of fluid (vof) method for the dynamics of free boundaries. *Journal of computational physics*, 39(1):201–225, 1981.

[19] Richard L Hoffman. A study of the advancing interface. i. interface shape in liquid-gas systems. *Journal of colloid and interface science*, 50(2):228–241, 1975.

[20] C. Huh and L.E Scriven. Hydrodynamic model of steady movement of a solid/liquid/fluid contact line. *Journal of Colloid and Interface Science*, 35(1):85–101, 1971.

[21] H Itō. Laminar flow in curved pipes. *ZAMM-Journal of Applied Mathematics and Mechanics/Zeitschrift für Angewandte Mathematik und Mechanik*, 49(11):653–663, 1969.

[22] Jr D.E. Jaekle. Propellant management device conceptual design and analysis-galleries. In *33rd Joint Propulsion Conference and Exhibit*, page 2811, 1997.

[23] Tsung-Shann Jiang, OH Soo-Gun, and John C Slattery. Correlation for dynamic contact angle. *Journal of Colloid and Interface Science*, 69(1):74–77, 1979.

[24] Stephan F. Kistler. Hydrodynamics of wetting. In John Berg, editor, *Wettability*, chapter 6, pages 311–430. Marcel Dekker, New York, New York, 1993.

[25] N. Kulev and M. Dreyer. Drop tower experiments on non-isothermal reorientation of cryogenic liquids. *Microgravity Science and Technology*, 22(4):463–474, 2010.

[26] N. Kulev, S. Basting, E. Bänsch, and M. Dreyer. Interface reorientation of cryogenic liquids under non-isothermal boundary conditions. *Cryogenics*, 62:48–59, 2014.

[27] D. Levine, B. Wise, R. Schulman, H. Gutierrez, D. Kirk, N. Turlesque, W. Tam, M. Bhatia, and D. Jaekle. Surface tension and contact angle analysis with design of propellant measurement apparatus. *Journal of Propulsion and Power*, 31(1):429–443, 2015.

[28] Sai Liu, Shanpeng Li, and Jianlin Liu. Jurin's law revisited: Exact meniscus shape and column height. *The European Physical Journal E*, 41(3), mar 2018. doi: 10.1140/epje/i2018-11648-1.

DOI: 10.13009/EUCASS2023-804

[29] Pedro Marques, Alessia Simonini, Laura Peveroni, and Miguel Alfonso Mendez. Experimental analysis of heat and mass transfer in non-isothermal sloshing using a model-based inverse method. *arXiv preprint arXiv:2212.12246*, 2022.

[30] Michael H Rausch, Lorenz Kretschmer, Stefan Will, Alfred Leipertz, and Andreas P Froba. Density, surface tension, and kinematic viscosity of hydrofluoroethers hfe-7000, hfe-7100, hfe-7200, hfe-7300, and hfe-7500. *Journal of chemical & engineering data*, 60(12):3759–3765, 2015.

[31] P Roura and Joaquim Fort. Local thermodynamic derivation of young's equation. *Journal of colloid and interface science*, 272(2):420–429, 2004.

[32] S. Schmitt and M. E Dreyer. Free surface oscillations of liquid hydrogen in microgravity conditions. *Cryogenics*, 72:22–35, 2015.

[33] Michael Stange, Michael E Dreyer, and Hans J Rath. Capillary driven flow in circular cylindrical tubes. *Physics of fluids*, 15(9):2587–2601, 2003.

[34] LH Tanner. The spreading of silicone oil drops on horizontal surfaces. *Journal of Physics D: Applied Physics*, 12 (9):1473, 1979.

[35] OV Voinov. Hydrodynamics of wetting. *Fluid dynamics*, 11(5):714–721, 1976.

[36] R Wanison, N Kimura, and M Murakami. A study of thermal performance change of cryogenic heat pipes by wick structures for wide range of working fluid filling ratio. *IOP Conference Series: Materials Science and Engineering*, 755(1):012109, mar 2020. doi: 10.1088/1757-899x/755/1/012109.

[37] Edward W. Washburn. The dynamics of capillary flow. *Physical Review*, 17(3):273–283, mar 1921. doi: 10.1103/physrev.17.273.

[38] Henry G Weller. Derivation, modelling and solution of the conditionally averaged two-phase flow equations. *Nabla Ltd, No Technical Report TR/HGW*, 2:9, 2002.

[39] Nicholas C White and Sandra M Troian. Why capillary flows in slender triangular grooves are so stable against disturbances. *Physical Review Fluids*, 4(5):054003, 2019.

[40] X. Zhong, B. Sun, and S. Liao. Analytic solutions of the rise dynamics of liquid in a vertical cylindrical capillary. *European Journal of Mechanics-B/Fluids*, 78:1–10, 2019.